
Localized Recombining Plasma in G166.0+4.3: A Supernova Remnant with an Unusual Morphology

Hideaki MATSUMURA¹, Hiroyuki UCHIDA¹, Takaaki TANAKA¹, Takeshi Go
TSURU¹, Masayoshi NOBUKAWA², Kumiko Kawabata NOBUKAWA³ and
Makoto ITOU¹

¹Department of Physics, Faculty of Science, Kyoto University, Kitashirakawa Oiwake-cho,
Sakyo-ku, Kyoto-shi, Kyoto 606-8502, Japan

²Science, Curriculum and Instruction, Faculty of Education, Nara University of Education,
Takabatake-cho, Nara-shi, Nara 630-8528, Japan

³Department of Physics, Nara Women's University, Kitauoyanishimachi, Nara 630-8506,
Japan

Received ; Accepted

Abstract

We observed the Galactic mixed-morphology supernova remnant G166.0+4.3 with Suzaku. The X-ray spectrum in the western part of the remnant is well represented by a one-component ionizing plasma model. The spectrum in the northeastern region can be explained by two components. One is the Fe-rich component with the electron temperature $kT_e = 0.87^{+0.02}_{-0.03}$ keV. The other is the recombining plasma component of lighter elements with $kT_e = 0.46 \pm 0.03$ keV, the initial temperature $kT_{init} = 3$ keV (fixed) and the ionization parameter $n_e t = (6.1^{+0.5}_{-0.4}) \times 10^{11}$ cm⁻³ s. As the formation process of the recombining plasma, two scenarios, the rarefaction and thermal conduction, are considered. The former would not be favored since we found the recombining plasma only in the northeastern region whereas the latter would explain the origin of the RP. In the latter scenario, an RP is anticipated in a part of the remnant where blast waves are in contact with cool dense gas. The emission measure suggests higher ambient gas density in the northeastern region. The morphology of the radio shell and a GeV gamma-ray emission also suggest a molecular cloud in the region.

Key words: X-rays: individual, G166.0+4.3, Recombining plasma

1 Introduction

Mixed-morphology supernova remnants (MM SNRs) have center-filled thermal X-ray emissions in a synchrotron radio shell (Rho & Petre 1998). Although the formation mechanism of the non-standard morphology has not been fully understood, there are two proposed scenarios. One is the evaporating cloudlet scenario (White & Long 1991), and the other is the thermal conduction scenario (Cox et al. 1999; Shelton et al. 1999). In either scenario, interactions between the blast wave and dense gas play an important role in the formation of

the X-ray morphology. Most MM SNRs are actually associated with molecular clouds as indicated by CO line emissions or OH (1720 MHz) masers (e.g., Lazendic & Slane 2006). They also exhibit GeV/TeV gamma-ray emissions which suggest shell-cloud interactions since those SNRs can emit luminous gamma rays through π^0 decays (e.g., Ackermann et al. 2013; Albert et al. 2007).

In the ASCA observation of the MM SNR IC 443, Kawasaki et al. (2002) measured ionization temperatures (T_z) based on the H-like to He-like $K\alpha$ intensity ratios of Si and S, and com-

pared them with electron temperatures (T_e). They found that T_z is significantly higher than T_e , and suggested that the plasma is overionized. In the observations of IC 443 (Yamaguchi et al. 2009) and W49B (Ozawa et al. 2009) with Suzaku, they discovered radiative recombining continua (RRC), which provide clear evidence that the plasmas are in an extremely recombining state. Subsequent Suzaku observations revealed recombining plasmas (RPs) in other MM SNRs in the Galaxy (e.g., G359.1–0.5: Ohnishi et al. 2011; W28: Sawada & Koyama 2012; W44: Uchida et al. 2012) as well as in the Large Magellanic Cloud (N49: Uchida, Koyama, Yamaguchi 2015).

Two scenarios are mainly considered for the formation process of the RPs. One is the rarefaction scenario (Itoh & Masai 1989). If a supernova explodes in a dense circumstellar matter (CSM) around the massive progenitor, ejecta and the CSM are shock-heated and quickly ionized because of the high density. When the shock breaks the CSM out to a lower density interstellar medium (ISM), T_e is decreased by adiabatic cooling. Kawasaki et al. (2002) proposed the other scenario, the thermal conduction scenario. If an SNR shock is interacting with a molecular cloud, thermal conduction occurs between the SNR plasma and the cloud, and, therefore, T_e drops. Since the recombination timescales of ions are generally longer than the conduction timescales, T_z cannot follow the decrease of T_e , and RPs can be realized.

G166.0+4.3 is a Galactic SNR whose radio shell has a large bipolar structure in the west with a smaller semicircle shell in the east (Sharpless 1959; Landecker et al. 1982; Pineault et al. 1987). Landecker et al. (1982) estimated the distance to G166.0+4.3 as 5.0 ± 0.5 kpc by using the Σ - D - z (surface brightness-diameter-distance above the Galactic plane) relationship. Pineault et al. (1987) suggested that the gas density in the east is higher than that in the west because of the unusual morphology of the radio shell. G166.0+4.3 was observed in the X-ray band with ROSAT (Burrows & Guo 1994), ASCA (Guo & Burrows 1997) and XMM-Newton (Bocchino et al. 2009). Burrows & Guo (1994) found the X-ray morphology is distinct from the radio morphology and reproduced the spectrum with collisional ionization equilibrium (CIE: $T_z = T_e$) models. They estimated the age of the remnant to be $\sim 2.4 \times 10^4$ yr by applying the evaporating cloudlet model (White & Long 1991) when they assume the estimated distance of 5 kpc. Bocchino et al. (2009) classified G166.0+4.3 as an MM SNR and reported that the spectra can be reproduced by an ionizing plasma (IP: $T_z < T_e$) model.

Gas environment of G166.0+4.3 is clearly different between the east and the west, according to the morphology of the radio shell. It is one of the best sources to study plasma evolution depending on the environment. In this paper, we report on observational results of G166.0+4.3 with Suzaku, which has high sensitivity and high energy resolution in the energy band of 0.3–

12 keV. We assume 5 kpc as the distance to the remnant in this paper.

2 Observations and data reduction

We performed Suzaku observations of G166.0+4.3. Table 1 summarizes the observation log. In this analysis, we used data from the X-ray Imaging Spectrometer (XIS: Koyama et al. 2007) installed on the focal planes of the X-ray telescopes (XRT: Serlemitsos et al. 2007). XIS2 and a part of XIS0 are not used in what follows. The former has not been functioning since 2006 November. The latter was turned off in 2009 June (Suzaku XIS documents^{1,2}).

We reduced the data using the HEADAS software version 6.19. We used the calibration database released in 2015 October for data processing. The total exposure time of the five observations is ~ 226 ks after the standard data screening. In the processing of the XIS data, we removed cumulative flickering pixels by referring to the noisy pixel maps³ provided by the XIS team. We also discarded pixels adjacent to the flickering pixels (pixel quality B14 = 1). Non X-ray backgrounds (NXBs) were estimated by `xisnxbgen` (Tawa et al. 2008). The redistribution matrix files and the ancillary response files were produced by `xismrfgen` and `xissimarfgen` (Ishisaki et al. 2007), respectively.

3 Analysis

3.1 Image

Figure 1 shows a mosaic image of G166.0+4.3 in the energy band of 0.5–2.0 keV. We subtracted the NXB from the image and corrected it for the vignetting effect of the XRT. Contours are a 325 MHz radio image from the Westerbord Northern Sky Survey (WENSS).

3.2 Background subtraction

For background estimation, we used Suzaku observational data of IRAS 05262+4432, which is located at $(l, b) = (165^\circ 1, 5^\circ 7)$. The observation log is shown in Table 1. We extracted a spectrum from a source-free region. In order to model the spectrum, we adopted a model by Masui et al. (2009). They observed the direction $(l, b) = (230^\circ, 0^\circ)$ with Suzaku in order to study the soft X-ray emission from the Galactic disk. Their model consists of four components: the cosmic X-ray background (CXB), the local hot bubble (LHB), and two thermal components for the Galactic halo (GH_{cold} and GH_{hot}).

¹ <http://www.astro.isas.ac.jp/suzaku/doc/suzakumemo/suzakumemo-2007-08.pdf>

² <http://www.astro.isas.ac.jp/suzaku/doc/suzakumemo/suzakumemo-2010-01.pdf>

³ <https://heasarc.gsfc.nasa.gov/docs/suzaku/analysis/xisnxbnew.html>

Table 1. Observation log.

Target	Obs. ID	Obs. date	(R.A., Dec.)	Effective Exposure
G166.0+4.3_NE	509022010	2014-Sep-19	(5 ^h 27 ^m 07 ^s .7, 42°58′52″.2)	61 ks
G166.0+4.3_NE	509022020	2014-Sep-22	(5 ^h 27 ^m 07 ^s .7, 42°58′52″.2)	61 ks
G166.0+4.3_NW	509023010	2014-Sep-20	(5 ^h 25 ^m 46 ^s .8, 42°54′01″.7)	42 ks
G166.0+4.3_SE	509024010	2014-Sep-21	(5 ^h 26 ^m 41 ^s .2, 42°39′06″.2)	34 ks
G166.0+4.3_SE	509024020	2015-Mar-13	(5 ^h 26 ^m 41 ^s .2, 42°39′06″.2)	27 ks
IRAS 05262+4432 (Background)	703019010	2008-Sep-14	(5 ^h 29 ^m 56 ^s .0, 44°34′39″.2)	82 ks

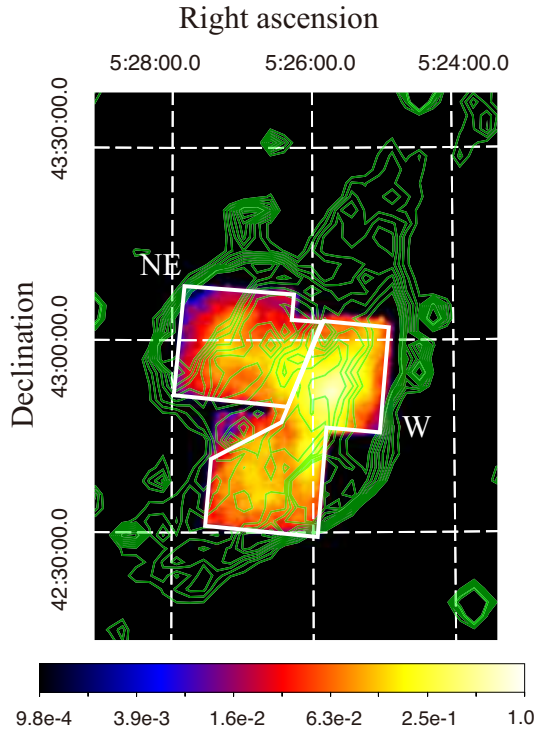


Fig. 1. XIS image of G166.0+4.3 in the 0.5–2.0 keV band after the NXB subtraction and the correction of the vignetting effect. The coordinates refer to epoch J2000.0. The X-ray count rate is normalized so that the peak becomes unity. We overlaid contours of the 325 MHz radio image from the WENSS.

We fit the background spectrum with the model after the NXB subtraction using XSPEC version 12.9.0. We fixed the electron temperatures of the LHB, GH_{cold} and GH_{hot} at the values by Masui et al. (2009). The absorption column density (N_{H}) of the CXB was fixed at $3.8 \times 10^{21} \text{ cm}^{-2}$, the Galactic value in the line of sight toward IRAS 05262+4432 (Dickey & Lockman 1990; Kalberla et al. 2005). The normalizations of all the components were allowed to vary. Figure 2 and Table 2 show the fitting result and the best-fit parameters, respectively.

3.3 SNR spectra

Considering the morphology of the radio shell, we extracted spectra from the northeast and west regions (named NE and W) indicated with the white solid lines in Figure 1. Figure 3 shows

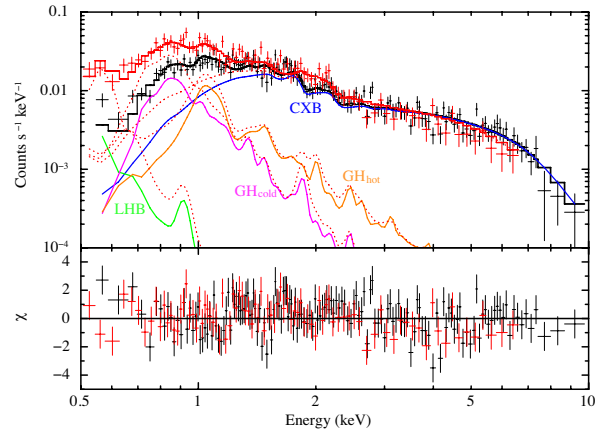


Fig. 2. XIS0+3 (black) and XIS1 (red) spectra taken from the source-free region of the IRAS 05262+4432 data with the best-fit model. The blue, green, magenta and orange lines represent the CXB, LHB, GH_{cold} and GH_{hot} models, respectively. The bottom panel shows the data residuals from the best-fit model.

Table 2. Best-fit model parameters of the background spectra

Component	Parameter (unit)	Value
CXB	N_{H} (10^{21} cm^{-2})	3.8 (fixed)
	Photon index	1.4 (fixed)
	Normalization*	10.7 ± 0.4
LHB	kT_e (keV)	0.105 (fixed)
	Normalization†	13.4 ± 3.2
GH_{cold}	kT_e (keV)	0.658 (fixed)
	Normalization†	2.1 ± 0.2
GH_{hot}	kT_e (keV)	1.50 (fixed)
	Normalization†	3.1 ± 0.5
χ^2 (d.o.f.)		301.9 (234)

*The unit is photons $\text{s}^{-1} \text{ cm}^{-2} \text{ keV}^{-1} \text{ sr}^{-1}$ @ 1 keV.

†The emission measure integrated over the line of sight, i.e., $(1/4\pi) \int n_e n_{\text{H}} dl$ in units of $10^{14} \text{ cm}^{-5} \text{ sr}^{-1}$.

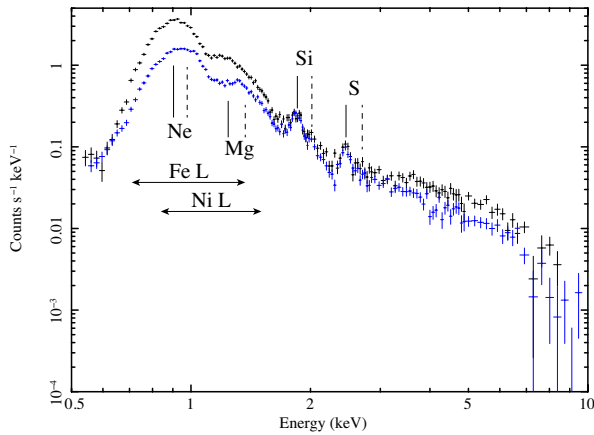


Fig. 3. XIS0+3 spectra of W (black) and NE (blue). The vertical solid and dashed black lines show the center energies of the K lines from He-like and H-like ions, respectively. The arrows indicate the energy bands with Fe-L and Ni-L line complexes.

XIS0+3 spectra of W and NE after the NXB subtraction. One can clearly see Fe-L and Ni-L line complexes, and Si-K and S-K lines. The Fe-L and Ni-L line complexes are more prominent in W than those in NE.

We fitted the spectra with the model consisting of the SNR component and the background (§3.2). The overall normalization of the background component was treated as a free parameter. The absorption column density of the CXB component was fixed at $3.6 \times 10^{21} \text{ cm}^{-2}$ which is the Galactic value in the line of sight toward G166.0+4.3.

We applied a one-component IP model to the W spectrum using the VVRNEI model in the XSPEC package, where the initial temperature (kT_{init}) is fixed at 0.01 keV whereas the electron temperature, ionization parameter ($n_e t$) and normalization are free parameters. We used the Wisconsin absorption model (Morrison & McCammon 1983) for the absorption whose column density is a free parameter. The abundances of O, Ne, Mg, Si, S, and Fe are also free parameters. The Ar and Ca abundances are linked to S, and Ni is linked to Fe. The abundances of the other elements are fixed to the solar values (Anders & Grevesse 1989). The energy band around the neutral Si K-edge (1.73–1.78 keV) is ignored because of the known calibration uncertainty. The fitting left large residuals around 0.82 keV and 1.23 keV due to the lack of Fe-L lines in the model (e.g., Yamaguchi et al. 2011). Therefore, we added two narrow lines at 0.82 keV and 1.23 keV. The results are shown in Figure 4 (w-i) and Table 3. We found that the spectrum is well reproduced by a one-component IP model with the electron temperature of 0.83 keV.

We applied the same IP model as W to the NE spectrum. Significant residuals are found at ~ 2.0 keV and ~ 2.6 keV which correspond to Si Ly α (2.0 keV) and the edge of the RRC of He-like Si (2.67 keV) + S Ly α (2.63 keV), respectively

(Figure 4 (ne-i)). These spectral features, if confirmed, provide evidence that the plasma is in a recombination-dominant state. We tried a one-component RP model. However, a satisfactory fit was not obtained.

For a detailed investigation, we restricted the energy band to > 1.6 keV where we found the large residuals, and tried one-component IP or RP models. The absorption column density is fixed to the best-fit value for W, $N_{\text{H}} = 0.8 \times 10^{21} \text{ cm}^{-2}$, whereas kT_e and $n_e t$ are left free. The kT_{init} is a free parameter for the RP model, whereas it is fixed at 0.01 keV for the IP model. The abundances of Si and S are free parameters, and those of Ar and Ca are linked to S. The residuals were not improved with the IP model (Figure 4 (ne-ii) and Table 3). On the other hand, we successfully fitted the spectrum with the RP model (Figure 4 (ne-iii) and Table 3).

We extrapolated the above RP model down to 0.5 keV. Figure 4 (ne-iv) shows the model and the full-band spectrum in the energy band of 0.5–10.0 keV. The spectral structure in the 0.7–1.1 keV band cannot be reproduced. With the electron temperature $kT_e = 0.37$ keV, the model predicts a peak energy of the Fe and Ni L line complexes at ~ 0.8 keV, which is significantly lower than the observed value of ~ 0.95 keV. Figure 5 shows the NE spectrum of XIS0+3 and the plasma model in the energy band of 0.5–1.2 keV. The model consists only of the Fe and Ni components with $N_{\text{H}} = 1.7 \times 10^{21} \text{ cm}^{-2}$, $kT_{init} = 3.0$ keV and $n_e t = 6.0 \times 10^{11} \text{ cm}^{-3} \text{ s}$. The electron temperatures are 0.40 keV and 0.85 keV in Figures 5 (a) and (b), respectively. The dominant emission lines of the Fe and Ni components are Fe xvii 2p5 3s1 \rightarrow 2p6 (0.725 keV and 0.739 keV) and Fe xvii 2p5 3d1 \rightarrow 2p6 (0.812 keV and 0.826 keV) with $kT_e = 0.40$ keV, and Fe xix 2p3 3s1 \rightarrow 2p4 (0.822 keV), Fe xviii 2p4 3d1 \rightarrow 2p5 (0.873 keV), Fe xx 2p2 3d1 \rightarrow 2p3 (0.965 keV) and Fe xxi 2p1 3d1 \rightarrow 2p2 (1.009 keV) with $kT_e = 0.85$ keV. The comparison between the data and the models indicates that the electron temperature of the Fe and Ni plasma should be ~ 0.85 keV in order to reproduce the observed structure. On the other hand, the Si and S plasma demands lower kT_e as we saw in the (ne-iii) fit.

The result indicates that the plasma has different kT_e between Fe (+Ni) and the other elements. Kamitsukasa et al. (2016) decomposed the ejecta of SNR G272.2–3.2 into components with different elements, considering that each element has different radial distributions. Following their idea, we adopted a two-component VVRNEI model: one for Fe and Ni, and the other for lighter elements. The spectra can be well fitted with the model comprising a CIE for Fe and Ni and an RP for the other elements. Figure 4 (ne-v) shows the spectrum with the best-fit model. Although we tried IP and RP for the Fe and Ni component, the ionization parameter $n_e t$ cannot be constrained well. Therefore, we here assumed the CIE model for simplicity.

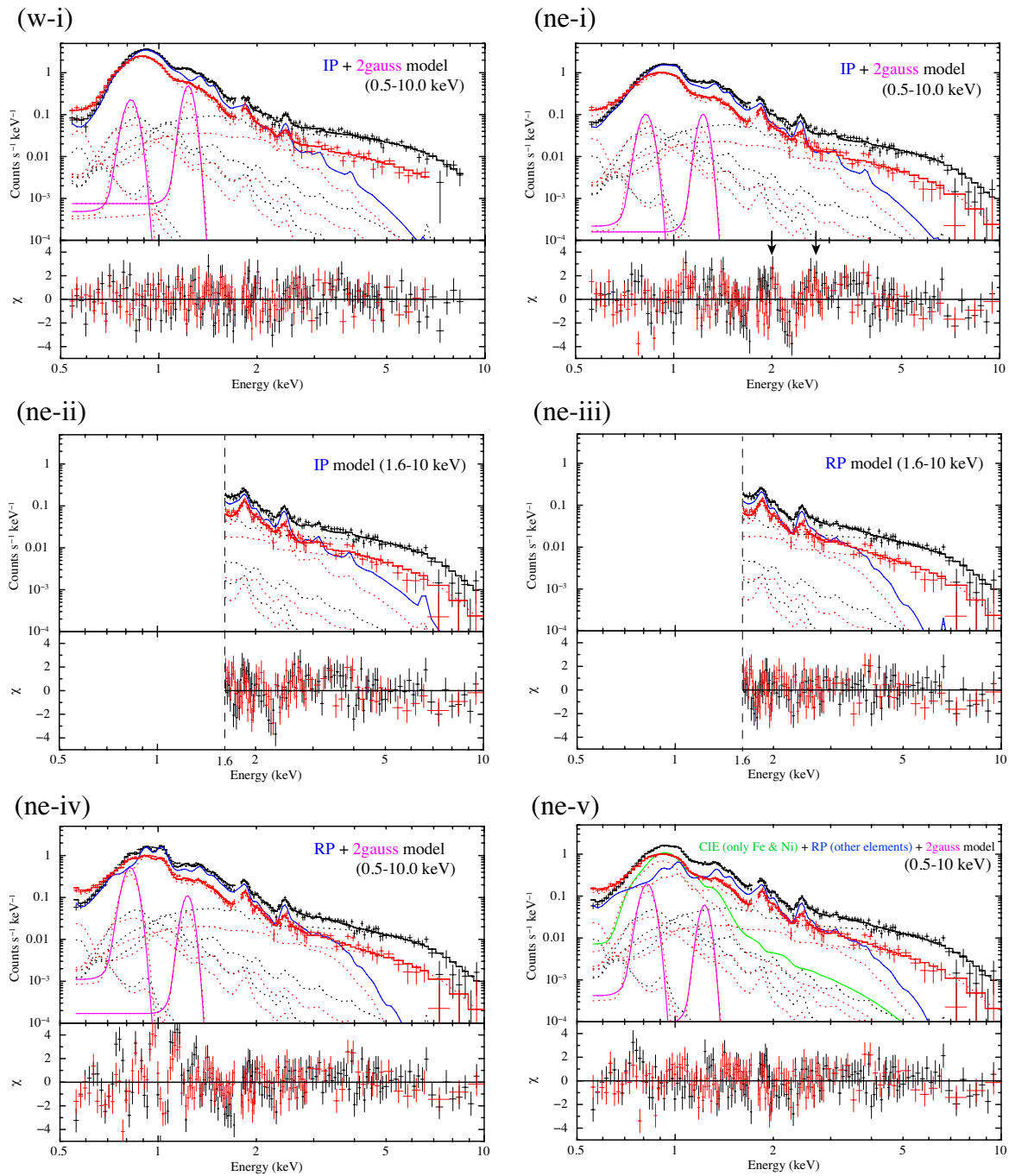


Fig. 4. XIS0+3 (black) and XIS1 (red) spectra of W or NE. Each spectrum is fitted with the plasma model (solid lines) and the background model (dotted lines).

Table 3. Fit parameters of source regions.

Model function	Parameter (unit)	(w-i)	(ne-i)	(ne-ii)	(ne-iii)	(ne-v)
Absorption	N_{H} (10^{21} cm^{-2})	0.8 ± 0.1	0.3 ± 0.1	0.8 (fixed)	0.8 (fixed)	1.7 ± 0.1
VVRNEI1	kT_e (keV)	0.83 ± 0.01	$0.90^{+0.01}_{-0.02}$	$1.36^{+0.51}_{-0.27}$	0.37 ± 0.04	0.46 ± 0.03
	kT_{init} (keV)	0.01 (fixed)	0.01 (fixed)	0.01 (fixed)	≥ 2.98	3.0 (fixed)
	H (solar)	1 (fixed)	1 (fixed)	1 (fixed)	1 (fixed)	1 (fixed)
	He (solar)	1 (fixed)	1 (fixed)	1 (fixed)	1 (fixed)	1 (fixed)
	C (solar)	1 (fixed)	1 (fixed)	1 (fixed)	1 (fixed)	1 (fixed)
	O (solar)	$0.4^{+0.2}_{-0.1}$	$0.2^{+0.2}_{-0.1}$	1 (fixed)	1 (fixed)	$0.02^{+0.03}_{-0.01}$
	Ne (solar)	$0.6^{+0.2}_{-0.1}$	$0.6^{+0.2}_{-0.1}$	1 (fixed)	1 (fixed)	0.4 ± 0.1
	Mg (solar)	1.2 ± 0.2	0.6 ± 0.1	1 (fixed)	1 (fixed)	0.6 ± 0.1
	Si (solar)	$0.7^{+0.1}_{-0.2}$	0.6 ± 0.1	$1.4^{+0.3}_{-0.1}$	2.3 ± 0.3	1.0 ± 0.1
	S = Ar = Ca (solar)	1.2 ± 0.3	1.2 ± 0.2	1.8 ± 0.4	$3.3^{+0.7}_{-0.6}$	1.5 ± 0.2
	Fe = Ni (solar)	1.2 ± 0.2	0.4 ± 0.1	1 (fixed)	1 (fixed)	—
	$n_e t$ ($10^{11} \text{ cm}^{-3} \text{ s}$)	$4.0^{+0.7}_{-0.5}$	3.1 ± 0.5	$1.6^{+1.7}_{-0.7}$	6.2 ± 0.6	$6.1^{+0.5}_{-0.4}$
	VEM (10^{57} cm^{-3}) [†]	2.7 ± 0.2	$2.9^{+0.2}_{-0.3}$	$1.2^{+0.3}_{-0.2}$	$6.6^{+1.6}_{-1.3}$	$10.3^{+0.8}_{-1.0}$
VVRNEI2	kT_e (keV)	—	—	—	—	$0.87^{+0.02}_{-0.03}$
	Fe = Ni (solar)	—	—	—	—	0.14 ± 0.01
	VEM (10^{57} cm^{-3}) [†]	—	—	—	—	= VVRNEI1
Gaussian	Centroid (keV)	0.82 (fixed)	0.82 (fixed)	—	—	0.82 (fixed)
	Normalization [‡]	$4.6^{+1.3}_{-0.7}$	$2.1^{+0.8}_{-0.7}$	—	—	$6.7^{+1.5}_{-1.3}$
Gaussian	Centroid (keV)	1.23 (fixed)	1.23 (fixed)	—	—	1.23 (fixed)
	Normalization [‡]	$3.4^{+1.3}_{-0.2}$	0.8 ± 0.1	—	—	0.7 ± 0.2
χ^2 (d.o.f.)		339.2 (247)	443.9 (251)	232.7 (150)	172.1 (150)	347.6 (250)

[†] Volume emission measure $\text{VEM} = \int n_e n_{\text{H}} dV$, where n_e , n_{H} , and V are the electron and hydrogen densities, and the emitting volume, respectively.

[‡] The unit is photons $\text{s}^{-1} \text{cm}^{-2} \text{sr}^{-1}$.

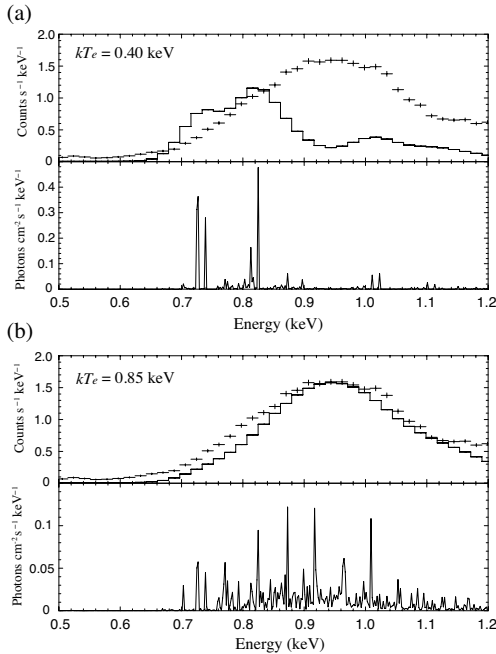


Fig. 5. (a) NE spectrum of XIS0+3 (crosses) and the plasma model with (top) and without (bottom) response matrices multiplied (solid lines) in the energy band of 0.5–1.2 keV. The plasma model consists only of Fe and Ni components with $N_{\text{H}} = 1.7 \times 10^{21} \text{ cm}^{-2}$, $kT_e = 0.40 \text{ keV}$, $kT_{\text{init}} = 3.0 \text{ keV}$ and $n_e t = 6.0 \times 10^{11} \text{ cm}^{-3} \text{ s}$. (b) Same as (a) but with $kT_e = 0.85 \text{ keV}$.

4 Discussion

4.1 Spatial structure

The spectral analysis shows that the NE plasma contains two components; the low temperature RP component and the high temperature Fe-rich component. This suggests that the distributions of the two components are different from each other. In order to investigate the distribution, we made XIS images in the Si-K band (1.75–2.10 keV) and the Fe-L band (0.70–1.30 keV). We divided them by the corresponding underlying continuum image for which we selected the line-free band of 1.50–1.70 keV. We show the images in Figure 6, which indicates that Si distributes uniformly whereas the Fe distribution is more compact. In some SNRs, regardless of the type of the explosion, distributions of Fe are observed to be centered (e.g., Uchida et al. 2009; Hayato et al. 2010). The observed distributions are consistent with the widely believed picture of supernova nucleosynthesis that heavier elements tend to be produced closer to the center of the progenitor.

For a detailed analysis of the Fe distribution, we extracted spectra from the three regions (i)–(iii) in NE indicated by the white lines in the bottom panel of Figure 6. We fitted the spectra of each region with the same model as Figure 4 (ne-v). We fixed kT_e of the RP component to the best-fit value, 0.46 keV. Figure 7 shows the resultant abundance ratios of Fe to Si. The ratio in the inner region is significantly higher and suggests the

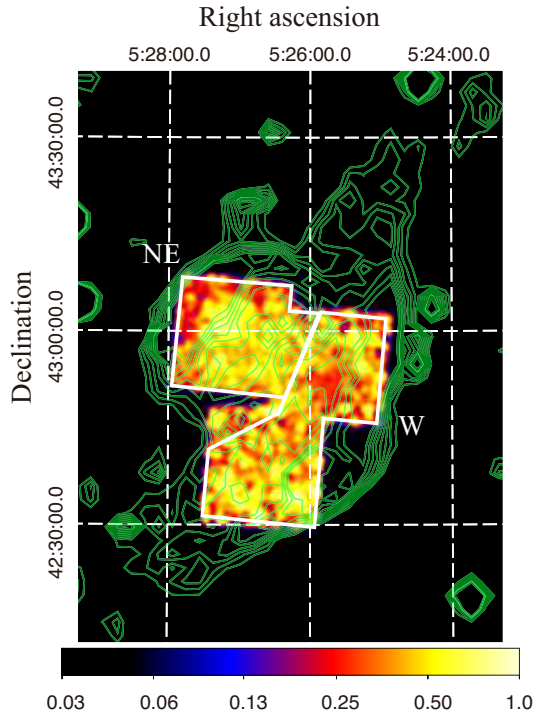


Fig. 6. XIS images of G166.0+4.3 in 1.75–2.10 keV band (Top: Si-K band) and the 0.70–1.30 keV band (Bottom: Fe-L and Ni-L band) after subtraction of the NXB and correction of the vignetting effect. The images are divided by the corresponding underlying continuum image for which we selected the line-free band of 1.50–1.70 keV. The scale is normalized so that the peak becomes unity. The contours are a radio image of the WENSS at 325 MHz.

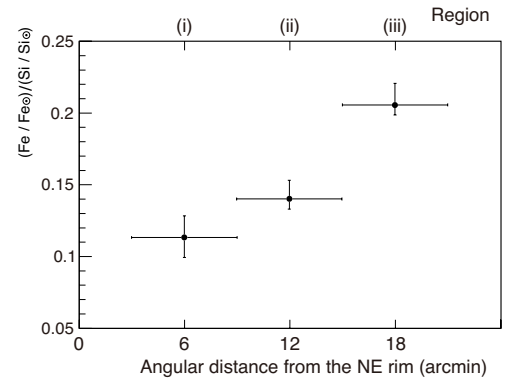


Fig. 7. Abundance ratios of Fe to Si in the regions (i)–(iii) as a function of angular distances from the NE rim toward the center of the remnant.

center-filled distribution of Fe.

4.2 Ambient gas density and SNR age

In our spectral analysis, the volume emission measures are $2.7 \times 10^{57} \text{ cm}^{-3}$ and $1.0 \times 10^{58} \text{ cm}^{-3}$ in W and NE, respectively. The volumes are obtained to be $4.1 \times 10^{59} f \text{ cm}^3$ and $1.8 \times 10^{59} f \text{ cm}^3$ for the W and NE plasmas, respectively, where f is the filling factor, assuming the morphologies to be prisms whose bases are the W and NE regions and depths are 40 pc and 20 pc for W and NE, respectively. With the volume emission measures, we obtain the electron densities $n_{e,W} = 0.3 (f/0.1)^{-1/2} \text{ cm}^{-3}$ and $n_{e,NE} = 0.9 (f/0.1)^{-1/2} \text{ cm}^{-3}$ for W and NE, respectively. They suggest that the ambient gas is denser in NE than that in W. This is supported by the radio morphology, the smaller shell in the eastern side. Another clue of denser gas in NE is the GeV gamma-ray emission detected in the eastern part of the remnant by Fermi LAT observations (Araya 2013). If π^0 decays are the main production process for the gamma rays, dense gas, which acts as targets for accelerated protons for π^0 production, would be in NE.

In the spectral analysis, we obtained $n_{e,W} t = 4.0 \times 10^{11} \text{ cm}^{-3} \text{ s}$ and $n_{e,NE} t = 6.1 \times 10^{11} \text{ cm}^{-3} \text{ s}$ for the W and NE plasmas, respectively. With $n_{e,W}$ and $n_{e,NE}$ calculated above based on the emission measures, the timescales are estimated to be $t = 1.4 \times 10^5 f^{1/2} \text{ yr}$ for W and $t = 7.1 \times 10^4 f^{1/2} \text{ yr}$ for NE. The ionization timescale for the W plasma, which is an IP, is expected to be almost the same as the age of the remnant, and, therefore, we estimate the age to be $t_{age} = 4 \times 10^4 (f/0.1)^{1/2} \text{ yr}$. With $n_{e,NE} t$, we can estimate the elapsed time since recombination started to dominate over ionization to be $t_{rec} = 2 \times 10^4 (f/0.1)^{1/2} \text{ yr} (< t_{age})$.

4.3 Origin of recombining plasma

The rarefaction (Itoh & Masai 1989) and thermal conduction (Kawasaki et al. 2002) scenarios have been considered for the formation process of RPs. In either case, the environment of the remnant is a key to the RP production process. We discovered an RP only in a part of G166.0+4.3, the outer part of the NE region, where the ambient gas is denser. In the W region, the spectrum is reproduced by the IP model. The different gas environments between the W and NE regions might be actually responsible for the difference of the plasma states.

In the rarefaction scenario, the electron temperature is decreased by adiabatic cooling when the blast wave breaks out of dense CSM into rarefied ISM. The lower the ISM density is, the more effective the adiabatic cooling must be (Shimizu et al. 2012). Therefore, in this scenario, we can naturally expect an RP in the W region whose ambient gas density would be lower. Our result, where we found an RP only in the NE region, is not simply explained by the rarefaction scenario.

In the thermal conduction scenario, an RP is anticipated in a part of the remnant where blast waves are in contact with cool dense gas. In the case of G166.0+4.3, the RP was discovered indeed in the denser NE region. In our results, the temperature of the inner Fe-rich plasma is higher ($kT_e = 0.87$ keV) than that of the outer RP ($kT_e = 0.46$ keV). In this scenario, the plasma is cooled from the outside layers. Therefore, it is possible that the plasma is cooled only in the outer part of the NE region.

5 Summary

We analyzed the Suzaku XIS data of SNR G166.0+4.3. The results we obtained are summarized as follows.

1. The plasma in the NE region consists of two components. One is the Fe-rich component with $kT_e = 0.87^{+0.02}_{-0.03}$ keV. The other is the RP component of the other lighter elements with $kT_e = 0.46 \pm 0.03$ keV, $kT_{init} = 3$ keV (fixed) and $n_e t = (6.1^{+0.5}_{-0.4}) \times 10^{11}$ cm⁻³ s.
2. The spectrum in the W region is well fitted with a one-component IP model with $kT_e = 0.83 \pm 0.01$ keV, $kT_{init} = 0.01$ keV (fixed) and $n_e t = (4.0^{+0.7}_{-0.5}) \times 10^{11}$ cm⁻³ s.
3. The Fe-rich plasma is concentrated near the center of the remnant whereas the other elements are distributed in the outer region.
4. Our results of the spectral analysis are not simply explained by the rarefaction scenario, whereas the origin of the RP would be explained by the thermal conduction with the cool dense gas in the northeastern part of the remnant.

Acknowledgments

The authors are grateful to Prof. Katsuji Koyama for helpful advice. We deeply appreciate all the Suzaku team members. We also thank the

WENSS team. This work is supported by JSPS Scientific Research grant numbers 15J01842 (H.M.), 15H02090, 26610047 and 25109004 (T.G.T.), 26800102 (H.U.), 25109004 (T.T.), and 16J00548 (K.K.N.).

References

- Ackermann, M., et al. 2013, *Science*, 339, 807
 Albert, J., et al. 2007, *ApJL*, 664, L87
 Anders, E., & Grevesse, N. 1989, *Geochim. Cosmochim. Acta*, 53, 197
 Araya, M. 2013, *MNRAS*, 434, 2202
 Bocchino, F., Miceli, M., & Troja, E. 2009, *A&A*, 498, 139
 Burrows, D. N., & Guo, Z. 1994, *ApJL*, 421, L19
 Cox, D. P., et al. 1999, *ApJ*, 524, 179
 Dickey, J. M., & Lockman, F. J. 1990, *ARA&A*, 28, 215
 Guo, Z., & Burrows, D. N. 1997, *ApJL*, 480, L51
 Hayato, A., et al. 2010, *ApJ*, 725, 894
 Ishisaki, Y., et al. 2007, *PASJ*, 59, 113
 Itoh, H., & Masai, K. 1989, *MNRAS*, 236, 885
 Kalberla, P. M. W., et al. 2005, *A&A*, 440, 775
 Kamitsukasa, F., et al. 2016, *PASJ*, 68, S7
 Kawasaki, M. T., et al. 2002, *ApJ*, 572, 897
 Koyama, K., et al. 2007, *PASJ*, 59, 23
 Landecker, T. L., Pineault, S., Routledge, D., & Vaneldik, J. F. 1982, *ApJL*, 261, L41
 Lazendic, J. S., & Slane, P. O. 2006, *ApJ*, 647, 350
 Masui, K., et al. 2009, *PASJ*, 61, S115
 Morrison, R., & McCammon, D. 1983, *ApJ*, 270, 119
 Ohnishi, T., et al. 2011, *PASJ*, 63, 527
 Ozawa, M., Koyama, K., Yamaguchi, H., Masai, K., & Tamagawa, T. 2009, *ApJL*, 706, L71
 Pineault, S., Landecker, T. L., & Routledge, D. 1987, *ApJ*, 315, 580
 Rho, J., & Petre, R. 1998, *ApJL*, 503, L167
 Sawada, M., & Koyama, K. 2012, *PASJ*, 64, 81
 Serlemitsos, P. J., et al. 2007, *PASJ*, 59, S9
 Sharpless, S. 1959, *ApJS*, 4, 257
 Shelton, R. L., et al. 1999, *ApJ*, 524, 192
 Shimizu, T., Masai, K., & Koyama, K. 2012, *PASJ*, 64, 24
 Tawa, N., et al. 2008, *PASJ*, 60, S11
 Uchida, H., Tsunemi, H., Katsuda, S., Kimura, M., & Kosugi, H. 2009, *PASJ*, 61, 301
 Uchida, H., et al. 2012, *PASJ*, 64, 141
 Uchida, H., Koyama, K., & Yamaguchi, H. 2015, *ApJ*, 808, 77
 White, R. L., & Long, K. S. 1991, *ApJ*, 373, 543
 Yamaguchi, H., et al. 2009, *ApJL*, 705, L6
 Yamaguchi, H., Koyama, K., & Uchida, H. 2011, *PASJ*, 63, S837